



UNIVERSITY OF LEEDS

This is a repository copy of *Innovative development of CuFe<sub>12</sub>O<sub>19</sub>-based ternary nanocomposites: Green synthesis, dual ZnO/Au modifications for enhanced photocatalytic degradation and antibacterial activity.*

White Rose Research Online URL for this paper:

<https://eprints.whiterose.ac.uk/226214/>

Version: Accepted Version

---

**Article:**

Hussein, N.M. and Mortazavi-Derazkola, S. orcid.org/0000-0002-1775-4525 (2025) Innovative development of CuFe<sub>12</sub>O<sub>19</sub>-based ternary nanocomposites: Green synthesis, dual ZnO/Au modifications for enhanced photocatalytic degradation and antibacterial activity. *Journal of Alloys and Compounds*, 1022. 179987. ISSN 0925-8388

<https://doi.org/10.1016/j.jallcom.2025.179987>

---

**Reuse**

This article is distributed under the terms of the Creative Commons Attribution (CC BY) licence. This licence allows you to distribute, remix, tweak, and build upon the work, even commercially, as long as you credit the authors for the original work. More information and the full terms of the licence here:

<https://creativecommons.org/licenses/>

**Takedown**

If you consider content in White Rose Research Online to be in breach of UK law, please notify us by emailing [eprints@whiterose.ac.uk](mailto:eprints@whiterose.ac.uk) including the URL of the record and the reason for the withdrawal request.



[eprints@whiterose.ac.uk](mailto:eprints@whiterose.ac.uk)  
<https://eprints.whiterose.ac.uk/>

# Innovative development of CuFe<sub>12</sub>O<sub>19</sub>-based ternary nanocomposites: green synthesis, dual ZnO/Au modifications for enhanced photocatalytic degradation and antibacterial activity

Nidal M. Hussein<sup>a</sup>, Sobhan Mortazavi-Drazkola<sup>b,c,\*</sup>

<sup>a</sup>*Department of Civil Engineering, Faculty of Engineering, University of Petra, Amman, Jordan*

<sup>b</sup>*Medical Toxicology and Drug Abuse Research Center (MTDRC), Birjand University of Medical Sciences, Birjand, Iran*

<sup>c</sup>*School of Chemistry and Astbury Centre for Structural Molecular Biology, University of Leeds, Leeds LS2 9JT, United Kingdom*

\*Corresponding author: Email: [S.mortazavi23@yahoo.com](mailto:S.mortazavi23@yahoo.com) and [S.mortazavi-derazkola@leeds.ac.uk](mailto:S.mortazavi-derazkola@leeds.ac.uk)

## Abstract

Antibiotic overuse and subsequent environmental contamination are significant threats to ecosystems and human health. To accomplish this objective, the CuFe<sub>12</sub>O<sub>19</sub>@ZnO/Au ternary nanocomposite (NCs) was synthesized using an eco-friendly, cost-efficient, and sustainable method. The synthesis, optimized using sodium dodecylbenzenesulfonate (SDBS) and *Valeriana officinalis* L. extract, resulted in uniform spherical nanoparticles ranging from 35-75 nm that confirmed with TEM, XRD, VSM, DRS, and FT-IR analyses. The photocatalytic efficiency of CuFe<sub>12</sub>O<sub>19</sub>@ZnO/Au was determined for the degradation of penicillin G under varying operational conditions. Under optimal conditions (pH 5, 20 ppm penicillin G concentration, and 0.8 g/L catalyst dosage), the nanocomposite revealed 89.61% degradation rate, outperforming CuFe<sub>12</sub>O<sub>19</sub> and CuFe<sub>12</sub>O<sub>19</sub>@ZnO. This enhancement is attributed to the reduced energy band gap of the magnetic substrate after the incorporation of ZnO and Au. Furthermore, the reusability test revealed that the nanocomposite maintained high degradation efficiency after five cycles. Antibacterial testing confirmed the strong antibacterial activity of the nanocomposite against Gram-negative bacteria, including *Escherichia*

*coli* and *Klebsiella pneumoniae*. This dual functionality, encompassing both photocatalytic degradation and antibacterial effects, positions CuFe<sub>12</sub>O<sub>19</sub>@ZnO/Au NCs as promising candidates for sustainable environmental remediation and antimicrobial applications.

Keyword: Nanocomposite; CuFe<sub>12</sub>O<sub>19</sub>; Green synthesis; Penicillin G; Antibacterial.

## 1. Introduction

Water is vital for life and must be pollutant-free. In developing countries, water pollution from contaminants like pharmaceuticals and heavy metals is a major environmental concern [1]. Pharmaceuticals, including antibiotics, enter the environment through wastewater from hospitals and factories. Their toxicity, persistence, and contribution to drug resistance make them stable pollutants [2]. Penicillin G (PG) is a water-soluble antibiotic produced by *Penicillium*, used to treat bacterial infections. It can persist in the environment, with residual concentrations reaching up to 1.68 mg L<sup>-1</sup> in treated wastewater. The persistence of PG in the environment, due to its non-biodegradability, highlights the need for efficient degradation methods to prevent contamination of aquatic ecosystems and mitigate health risks associated with antibiotic exposure [3, 4].

Conventional treatment methods for removing pharmaceutical pollutants are often inefficient due to the presence of aromatic rings in their molecular structure. Advanced Oxidation Processes (AOPs), particularly ultraviolet-based AOPs, present a promising solution for addressing water contamination caused by emerging organic pollutants [4, 5]. Photocatalytic methods offer eco-friendly solutions for removing organic pollutants, effectively avoiding secondary pollution [6]. Various nanomaterials, such as MgFe<sub>2</sub>O<sub>4</sub> [7], CuAl<sub>2</sub>O<sub>4</sub> [8], and MnO<sub>2</sub> [9], have been used for pollutant degradation, all of which have demonstrated satisfactory results in pollutant removal.

Hexaferrites, particularly MFe<sub>12</sub>O<sub>19</sub> (where M can be a divalent metal such as Cu<sup>2+</sup>, Zn<sup>2+</sup>, Ba<sup>2+</sup>, and others), are highly regarded for their unique magnetic and photocatalytic properties. These materials have been extensively studied due to their stability, low cost, and versatile applications in fields such

as magnetic recording, high-frequency devices, and photocatalysis [10, 11].  $\text{MFe}_{12}\text{O}_{19}$  compounds can be fabricated via different processes, such as hydrothermal and sol-gel, ensuring the formation of homogeneous nanostructures with controlled morphology [12-14]. Among these,  $\text{CuFe}_{12}\text{O}_{19}$  has been considered in this study due to its potential for improved charge separation, which may contribute to reduced electron-hole recombination and enhanced photocatalytic efficiency. A previous study have demonstrated that  $\text{CuFe}_{12}\text{O}_{19}$  exhibits excellent photocatalytic activity when combined with carbon-based materials such as CNTs and graphene [11]. However, further modifications are required to optimize its performance, particularly in aqueous environments where charge recombination and limited surface activity can reduce efficiency.

To address these challenges,  $\text{CuFe}_{12}\text{O}_{19}$  was coupled with ZnO and Au to form a ternary nanocomposite with improved photocatalytic and antibacterial properties. ZnO is a well-known photocatalyst with a wide bandgap making it highly effective in pollutant degradation [15, 16]. By integrating ZnO with  $\text{CuFe}_{12}\text{O}_{19}$ , we aim to enhance charge separation and extend the photocatalytic activity under UV light irradiation. Furthermore, the deposition of gold nanoparticles (AuNPs) onto the  $\text{CuFe}_{12}\text{O}_{19}$ @ZnO composite introduces additional advantages. AuNPs are known for their unique optical properties [17], which can improve light absorption through surface plasmon resonance (SPR) [18] and facilitate charge transfer at the interface, ultimately enhancing the photocatalytic efficiency. In this research, the rationale behind incorporating AuNPs is twofold: (i) they act as electron sinks, thereby reducing charge carrier recombination and extending the lifetime of reactive species [19], and (ii) they enhance light absorption through localized LSPR effects, further boosting photocatalytic performance. Chen's study reported that the increased absorption was attributed to the SPR effect of gold nanoparticles [20]. Additionally, while gold nanoparticles are known to sometimes promote charge recombination, their role in photocatalysis is largely dependent on factors such as particle size, deposition method, and material architecture.

Herein, we synthesized novel three-component nanocomposites to investigate their photocatalytic and antibacterial activities. Several key innovations of this work are as follows: (i) Synthesis of  $\text{CuFe}_{12}\text{O}_{19}@Z\text{nO}/\text{Au}$  NCs for the first time. (ii) Utilization of *Valeriana officinalis* L. plant extract for the reduction of  $\text{Au}^{3+}$  and the synthesis of nanocomposites. (iii) Adoption of a green and cost-effective method for the synthesis of the nanocomposites. (iv) Exploration of various conditions to obtain the highest degradation performance of the antibiotic Penicillin G. These novel approaches contribute to the advancement of photocatalysis and antibacterial studies, offering new insights into sustainable material synthesis and effective antibiotic degradation.

## 2. Experimental

### 2.1. Materials

The precursors used in this study included iron (III) nitrate nonahydrate, sodium dodecylbenzenesulfonate, tetrachloroauric (III) acid trihydrate, zinc nitrate hexahydrate, copper (II) nitrate hexahydrate, methanol, and ethanol were purchased from Sigma-Aldrich that analytical grade without further purification. Additionally, double-distilled water was employed throughout the experiments.

### 2.2. Preparation of *Valeriana officinalis* L. extract

The *Valeriana officinalis* L. plant was collected from the forests of Mazandaran Province, Iran. After thorough washing and removal of any debris, the plant was dried for 48 h. Extraction was carried out according to the method explained by Mohammadi-Aghdam et al., with slight modification [21]. In this process, 250 g of the powdered *Valeriana officinalis* was immersed in methanol. The mixture was left to soak in methanol for 72 h. After this soaking period, the solvent was evaporated using a rotary equipment. The resulting extract was stored at 4°C.

### 2.3. Fabrication of magnetic $\text{CuFe}_{12}\text{O}_{19}$ nanoparticles

CuFe<sub>12</sub>O<sub>19</sub> nanoparticles were fabricated using the auto-combustion sol-gel process, based on a procedure previously reported by Ansari et al., with slight modifications [10]. In this synthesis, sodium dodecylbenzenesulfonate was used as a capping agent, and citric acid (C<sub>6</sub>H<sub>8</sub>O<sub>7</sub>) served as a fuel to facilitate the auto-combustion process. Initially, 0.3 g of Cu(NO<sub>3</sub>)<sub>2</sub>·6H<sub>2</sub>O was dissolved in 10 mL of H<sub>2</sub>O. Then, 10 mL of SDBS (with a molar ratio 1:1 Cu:SDBS) was added dropwise to the copper solution while stirring gently. The reaction was allowed to continue for 30 min. Next, a stoichiometrically balanced amount of citric acid was added to maintain the appropriate fuel-to-oxidizer (F/O) ratio in the mixture. Subsequently, 15 mL of distilled water containing iron nitrate (Fe(NO<sub>3</sub>)<sub>3</sub>·9H<sub>2</sub>O) was added dropwise (one drop every 5 seconds) to the reaction mixture in a molar ratio of 1:12 (Cu:Fe). The reaction was conducted at 100 °C with vigorous stirring for 50 min. During this stage, the solution gradually transformed into a viscous gel due to the complexation of metal ions with citric acid and the progressive evaporation of water. The gel was dried at 120 °C and subjected to calcination in a furnace at 950 °C for 3 h to obtain phase-pure CuFe<sub>12</sub>O<sub>19</sub> nanoparticles.

#### *2.4. Fabrication of magnetic CuFe<sub>12</sub>O<sub>19</sub>@ZnO NCs*

Initially, 200 mg of CuFe<sub>12</sub>O<sub>19</sub> nanoparticles were dispersed in 20 mL of ethanol and water solution under ultrasonic conditions. Next, a specific amount of SDBS was dissolved in 15 mL of water and added to the CuFe<sub>12</sub>O<sub>19</sub> solution. The SDBS surfactant playing a crucial role in obtaining uniform and homogeneous nanomaterials. To facilitate deposition, a 10% zinc oxide salt (Zn(NO<sub>3</sub>)<sub>2</sub>·6H<sub>2</sub>O) solution was prepared by dissolving a specific amount of zinc salt in 10 mL of water and adding it to the solution. By adding 0.8 M sodium hydroxide, the pH of the solution was subsequently adjusted to 12. A color change from nearly black to a lighter black indicated the preparation of Zn(OH)<sub>2</sub> on the CuFe<sub>12</sub>O<sub>19</sub>. Finally, the obtained powder was calcined at 550°C for 3 h to obtain the CuFe<sub>12</sub>O<sub>19</sub>@ZnO NCs.

#### *2.5. Fabrication of CuFe<sub>12</sub>O<sub>19</sub>@ZnO/Au NCs*

To introduce gold nanoparticles onto the magnetic substrate, 7 mg of gold chloride, dissolved in 5 mL of distilled water, were slowly introduced into the CuFe<sub>12</sub>O<sub>19</sub>@ZnO NCs while stirring at a low speed. Subsequently, 5 mL of *Valeriana officinalis L.* extract was introduced dropwise into the solution. The extract served a dual function: it acted as a reducing agent, facilitating the reduction of gold ions to gold nanoparticles, and as a stabilizing agent, ensuring the stability and uniform dispersion of the formed nanoparticles. After 60 min, the mixture was centrifuged and then dried

### 2.6. Antibacterial activity

In this study, the antibacterial performance of the synthesized nanocomposites was evaluated according to the method proposed by Kiani et al. [22]. As the primary focus of this research was on the photocatalytic properties of the nanocomposites, the antibacterial test was conducted as a supplementary analysis to assess any potential antibacterial effects of the synthesized material. Given the composition of the nanocomposite, strong antibacterial activity was not expected. To compare the antibacterial potential, tetracycline, a well-known antibiotic, was used as a reference. The antibacterial test was performed against four bacterial strains, including two Gram-positive bacteria (*Staphylococcus aureus* and *Enterococcus faecalis*) and two Gram-negative bacteria (*Escherichia coli* and *Klebsiella pneumoniae*). For the antibacterial assay, 100 µL of Muller-Hinton broth medium containing various concentrations of the NCs were added to microplate. Then, 100 µL of bacterial suspension was introduced into each well. The experiments were carried out in triplicate. Following 24 h, the minimum inhibitory concentration (MIC) was evaluated by observing the turbidity of the wells. The lowest concentration that showed no turbidity was considered the MIC.

### 2.7. Photocatalytic test

The photocatalytic degradation was carried out under UV-C light using a radiation source with a wavelength of 253.7 nm (18 W). The absorbance of Penicillin G, as an antibiotic pollutant, was recorded at 225 nm, which corresponds to its maximum absorption wavelength ( $\lambda_{\text{max}}$ ), using a UV-

UV-Vis instrument. Optimization of the degradation process was performed to achieve the highest efficiency, considering various parameters, including nanocatalyst concentration (0.2-1.7 g/L), antibiotic concentration (20-80 mg/L), and pH (1-11). First, a known concentration of the penicillin G was diluted in 30 mL of distilled water. A set amount of nanomaterials was then introduced into the solution. Then, at designated time points, solution samples were taken, and their absorbance was determined with UV-Vis instrument. Sampling was performed at 140 min intervals. [Table. 1](#) provides the details of this experiments. The degradation of Penicillin G was measured based on the following equation.  $A_0 - A_t / A_0 \times 100$ .  $A_0$  is the absorbance at initial time and  $A_t$  is the absorbance after  $t$  time.

### 3. Results and discussion

#### 3.1. Suggested mechanism for $Au^{3+}$ reduction

One critical aspect of this study is understanding the mechanism behind the reduction of  $Au^{3+}$  on the surface of  $CuFe_{12}O_{19}@ZnO$  nanocomposites and the subsequent formation of AuNPs using *Valeriana officinalis L.* extract. While the exact concentrations of phenolic compounds in the extract were not determined in this study, previous reports have shown that gallic acid is one of the most abundant phenolic compounds in *Valeriana officinalis L.* extract (e.g., [\[23\]](#)). Based on these findings, we propose that gallic acid may play a significant role in the reduction of gold ions, leading to the formation of  $Au^{3+}$  on the surface of  $CuFe_{12}O_{19}@ZnO$  NCs. The suggested mechanism is depicted in [Fig. 1](#). It is important to note that this mechanism is based on literature evidence, and further studies are required to confirm the exact role of gallic acid and other phenolic compounds in this process.

#### 3.2. XRD analysis

The crystalline structure of the fabricated materials was examined using X-ray diffraction (XRD) analysis. The XRD patterns for  $CuFe_{12}O_{19}$  nanoparticles, as well as for the  $CuFe_{12}O_{19}@ZnO$  and  $CuFe_{12}O_{19}@ZnO/Au$  NCs, are shown in [Figure 2](#). The XRD pattern for  $CuFe_{12}O_{19}$ , shown in [Fig. 2a](#),

does not match any standard JCPDS reference card, which is expected, as this compound is relatively new and has not yet been assigned an official reference pattern. We hypothesize that the synthesized material may consist of a combination of  $\text{Fe}_2\text{O}_3$  and  $\text{CuFe}_2\text{O}_4$ , as the single crystal of  $\text{CuFe}_{12}\text{O}_{19}$  has not yet been isolated, and thus, its exact composition remains uncertain. However, similar diffraction patterns have been reported in the literature. Mahdiani et al. [11] observed an XRD pattern for  $\text{CuFe}_{12}\text{O}_{19}$  that could not be identified using JCPDS cards, confirming its phase purity by comparing it with the reference provided by Ansari et al. [10]. Our results are in strong agreement with these previously reported XRD patterns, confirming the successful synthesis of  $\text{CuFe}_{12}\text{O}_{19}$  in this study. Upon incorporation of ZnO onto the  $\text{CuFe}_{12}\text{O}_{19}$ , nine additional peaks were detected, as shown in Fig. 2b. These peaks correspond to ZnO and are located at  $31.89^\circ$  (100),  $34.21^\circ$  (002),  $36.12^\circ$  (101),  $47.52^\circ$  (102),  $56.72^\circ$  (110),  $62.52^\circ$  (103),  $68.07^\circ$  (112), and  $77.51^\circ$  (202). These results confirm the presence of ZnO in the composite and align well with the JCPDS reference card (01-080-0075). Finally, the XRD pattern for the  $\text{CuFe}_{12}\text{O}_{19}@ZnO/Au$  NCs is presented in Fig. 2c. The presence of Au in the composite is confirmed by four distinct peaks at  $38.32^\circ$  (111),  $44.34^\circ$  (200),  $64.26^\circ$  (220), and  $77.49^\circ$  (311). These peaks are characteristic of face-centered cubic gold and match well with the JCPDS reference card (00-004-0784). Gold nanoparticles were formed on the magnetic substrate using *Valeriana officinalis* L. extract, which acts as both a reducing and stabilizing agent. Our results were consistent with the findings reported by Sundararajan et al. [24]. They demonstrated that the green-synthesized gold nanoparticles exhibited four main peaks at  $38.18^\circ$ ,  $44.38^\circ$ ,  $64.57^\circ$ , and  $77.56^\circ$ .

### 3.3. FT-IR spectra

FT-IR spectroscopy was employed in this study to analyze the functional groups present in the synthesized materials. Figure 3 presents the FT-IR spectra of  $\text{CuFe}_{12}\text{O}_{19}$ ,  $\text{CuFe}_{12}\text{O}_{19}@ZnO$ , and  $\text{CuFe}_{12}\text{O}_{19}@ZnO/Au$  NCs. The FT-IR spectrum of  $\text{CuFe}_{12}\text{O}_{19}$  (Fig. 3a) exhibits an absorption band at  $3432$  and  $1642\text{ cm}^{-1}$ , corresponding to the hydroxyl stretching vibrations of water molecules [11, 25, 26], likely due to surface hydroxylation caused by ambient humidity during sample preparation.

Additionally, weak absorption peaks in the range of 1000-1200  $\text{cm}^{-1}$  indicate the presence of residual nitrate groups from precursor materials [11]. The strong absorption bands at 474  $\text{cm}^{-1}$  and 569  $\text{cm}^{-1}$  correspond to Fe-O and Cu-O stretching vibrations, verifying the presence of metal-oxygen bonds [11]. The FT-IR spectrum of  $\text{CuFe}_{12}\text{O}_{19}@ZnO$  NCs (Fig. 3b) reveals similar metal-oxygen bonds at 466  $\text{cm}^{-1}$  and 553  $\text{cm}^{-1}$ . However, the intensity of these bands slightly decreases due to the incorporation of ZnO nanoparticles. A new absorption band at 579  $\text{cm}^{-1}$  is related with Zn-O stretching vibrations [21]. Furthermore, bands at 2931 and 3408  $\text{cm}^{-1}$  correspond to C-H and hydroxyl stretching vibrations, respectively [27], with the latter likely arising from adsorbed moisture on the nanocomposite surface. The FT-IR spectrum of  $\text{CuFe}_{12}\text{O}_{19}@ZnO/Au$  NCs (Fig. 3c) exhibits spectral features corresponding to the functional groups of *Valeriana officinalis* L. extract, which was applied as a reducing agent for gold ion reduction and gold nanoparticle formation on the magnetic substrate. Absorption bands below 1000  $\text{cm}^{-1}$  correspond to metal-oxygen bonds related to  $\text{CuFe}_{12}\text{O}_{19}$  and ZnO, while a broad band at 3419  $\text{cm}^{-1}$  represents O-H stretching vibrations. Additionally, strong absorption peaks at 1687 and 1051  $\text{cm}^{-1}$  are attributed to carbonyl group (C=O), and -C-O stretching vibrations of alcohol groups, respectively [28], confirming the successful incorporation of extract-derived functional groups. These findings validate the successful synthesis of  $\text{CuFe}_{12}\text{O}_{19}@ZnO/Au$  NCs.

### 3.4. Morphology and size study

The morphology, size, and uniformity of the synthesized products were evaluated using TEM analysis. Fig. 4 presents TEM images and histograms of the particle size distribution for the  $\text{CuFe}_{12}\text{O}_{19}$ ,  $\text{CuFe}_{12}\text{O}_{19}@ZnO$ , and  $\text{CuFe}_{12}\text{O}_{19}@ZnO/Au$  NCs. As shown, the particle size increased with the addition of each new component. The  $\text{CuFe}_{12}\text{O}_{19}$  nanoparticles (Fig. 4a) exhibit a size range of 15-45 nm, which is confirmed by histogram analysis. Some degree of agglomeration can be attributed to the magnetic nature of the nanoparticles. A similar particle size (~35-40 nm) was reported in a study by Javidan et al., where  $\text{CuFe}_{12}\text{O}_{19}$  was fabricated using the co-precipitation method [29]. Upon adding ZnO nanoparticles onto the magnetic  $\text{CuFe}_{12}\text{O}_{19}$  substrate, the particle size increased to

25-60 nm (Fig. 4b). Some areas displayed partial agglomeration due to the composite's magnetic properties, which occasionally explain the larger particle sizes observed in the histogram. Similar results were reported by Asri et al., where the deposition of zinc oxide on a magnetic substrate led to an increase in particle size [30]. After incorporating gold nanoparticles using *Valeriana officinalis* L. extract, the particle size slightly increased. TEM images of the nanocomposites show oval-shaped nanoparticles (Fig. 4c) with sizes ranging from 35 to 75 nm. The presence of the extract on the gold nanoparticles led to mild aggregation, although individual nanocomposites remain distinguishable. Overall, the synthesized nanocomposites exhibit spherical morphology and suitable size, indicating their potential for catalytic and biological applications.

### 3.5. Magnetic properties of nanocatalysts

Magnetic properties are among the most critical characteristics of nanomaterials, facilitating their separation and reuse, particularly in environmentally focused applications. To assess the magnetic behavior of the synthesized nanocatalysts, Vibrating Sample Magnetometry (VSM) was performed. The VSM results for  $\text{CuFe}_{12}\text{O}_{19}$ ,  $\text{CuFe}_{12}\text{O}_{19}@\text{ZnO}$ , and  $\text{CuFe}_{12}\text{O}_{19}@\text{ZnO}/\text{Au}$  NCs are presented in Fig. 5, revealing saturation magnetization ( $M_s$ ) values of 13.27 (Fig. 5a), 8.11 (Fig. 5b), and 3.96 emu/g (Fig. 5c), respectively. The observed decrease in  $M_s$  values following the deposition process is related to the non-magnetic nature of ZnO and Au NPs. Despite this reduction, both  $\text{CuFe}_{12}\text{O}_{19}@\text{ZnO}$  and  $\text{CuFe}_{12}\text{O}_{19}@\text{ZnO}/\text{Au}$  retained sufficient magnetic properties, allowing for their effective separation from aqueous solutions using an external magnet. This confirms their potential as recyclable and environmentally friendly magnetic nanocatalysts. Furthermore, the synthesis of  $\text{CuFe}_{12}\text{O}_{19}@\text{ZnO}/\text{Au}$  NCs using *Valeriana officinalis* L. extract reinforces their applicability as green catalysts, offering both recyclability and efficiency in various catalytic processes.

### 3.6. DRS analysis

The photocatalytic activity of nanocomposites is significantly influenced by their ability to absorb light and their bandgap energy ( $E_g$ ). In this study, diffuse reflectance spectroscopy (DRS) was used to evaluate the electronic structure and light absorption properties of the synthesized nanocomposites. The results showed (Fig. 6) that the bandgap values for  $\text{CuFe}_{12}\text{O}_{19}$ ,  $\text{CuFe}_{12}\text{O}_{19}@\text{ZnO}$ , and  $\text{CuFe}_{12}\text{O}_{19}@\text{ZnO}/\text{Au}$  NCs were 3.26, 3.14, and 3.02 eV, respectively. The observed reduction in the bandgap of the  $\text{CuFe}_{12}\text{O}_{19}@\text{ZnO}/\text{Au}$  NCs is attributed to the synergistic effects of ZnO and Au nanoparticles. The incorporation of ZnO leads to improved charge separation at the heterojunction interface, while Au nanoparticles enhance light absorption, particularly in the visible range, due to the localized surface plasmon resonance (LSPR) effect. Furthermore, Au acts as an electron sink, facilitating charge transfer and reducing electron-hole recombination, which has been demonstrated in previous studies [31]. These combined effects contribute to the observed decrease in the effective bandgap, enhancing the photocatalytic efficiency of the nanocomposite under UV light.

### 3.7. Antibacterial activity

The antibacterial performance of  $\text{CuFe}_{12}\text{O}_{19}$ ,  $\text{CuFe}_{12}\text{O}_{19}@\text{ZnO}$ , and  $\text{CuFe}_{12}\text{O}_{19}@\text{ZnO}/\text{Au}$  NCs was evaluated against four bacterial strains. The results, summarized in Table. 2, indicate that  $\text{CuFe}_{12}\text{O}_{19}$  alone exhibited negligible antibacterial activity (MIC > 4000  $\mu\text{g}/\text{mL}$ ), likely due to its lack of intrinsic bactericidal properties. However, ZnO deposition significantly enhanced antibacterial efficacy, as evidenced by the reduced MIC values of 1000, 2000, 2000, and 2000  $\mu\text{g}/\text{mL}$  for *Escherichia coli*, *Klebsiella pneumoniae*, *Enterococcus faecalis*, and *Staphylococcus aureus*, respectively. The incorporation of gold nanoparticles into  $\text{CuFe}_{12}\text{O}_{19}@\text{ZnO}$  NCs further enhanced antibacterial performance, with MIC values decreasing to 500, 500, 1000, and 1000  $\mu\text{g}/\text{mL}$  for the respective bacterial strains. This improvement can be attributed to the ability of gold nanoparticles to increase cellular uptake and intensify ROS-mediated stress. Furthermore, the use of *Valeriana officinalis* L. extract in the synthesis process likely contributed to improved surface characteristics and biocompatibility. This extract contains bioactive compounds, such as polyphenols and flavonoids,

which may aid in stabilizing nanoparticles and enhancing their antibacterial effects. The higher susceptibility of Gram-negative bacteria to these nanocomposites can be attributed to their thinner peptidoglycan layers [32], which facilitate better nanoparticle penetration. In contrast, Gram-positive bacteria exhibit greater resistance due to their thicker cell walls. The proposed antibacterial mechanism, supported by previous studies [22], involves the adhesion of nanomaterials to bacterial membranes, causing membrane disruption and pore formation. This allows nanomaterials to penetrate the bacterial cell, where they interact with intracellular components and induce oxidative stress via ROS generation, ultimately leading to bacterial cell death (Fig. 7).

### 3.8. Photocatalytic degradation

This study investigates the use of NCs for the degradation of the Penicillin G. Our approach involved determining the optimal dose of the nanocatalyst,  $\text{CuFe}_{12}\text{O}_{19}$ , pH, and pollutant concentration, followed by evaluating the photocatalytic activity of  $\text{CuFe}_{12}\text{O}_{19}@\text{ZnO}$  and  $\text{CuFe}_{12}\text{O}_{19}@\text{ZnO}/\text{Au}$  under these optimal conditions. To evaluate the effect of UV-C radiation alone, a control experiment was conducted without the nanocatalyst. The results showed that after 140 min of UV-C exposure, only ~4.3% of Penicillin G was degraded, indicating that direct photolysis is not significantly effective. This highlights the necessity of a photocatalyst to enhance degradation efficiency.

#### 3.8.1. Effect of pH

The pH of the reaction medium plays a crucial role in the degradation efficiency of pollutants. In this study, pH values of 1, 3, 5, 7, and 11 were tested to identify the optimal condition. As illustrates in Fig. 8, the best degradation was observed at pH 5, with the lowest degradation occurring at pH 1 (catalyst concentration 0.5 g/L and antibiotic concentration 40 ppm). As the pH increased from 1 to 5, the degradation efficiency increased from 17.61% at pH 1 to 60.84% at pH 5. However, further increases in pH beyond 5 resulted in a decrease in degradation efficiency, with pH 11 showing a reduction to 47.72%. This behavior can be explained by the interaction between the nanocatalyst

surface and ions in the solution. At pH values below 5, the surface of  $\text{CuFe}_{12}\text{O}_{19}$  is predominantly occupied by  $\text{H}^+$  ions, resulting in a positive surface charge. In contrast, at pH values above 5,  $\text{OH}^-$  ions dominate the surface, leading to a negative charge. Under basic conditions, Penicillin G transitions into its anionic form, leading to electrostatic repulsion with the negatively charged catalyst surface. This electrostatic repulsion hinders effective interaction between the catalyst and the antibiotic, leading to a decrease in degradation efficiency [33]. Furthermore, at lower pH values, hydroxyl radicals are less hindered by  $\text{H}^+$  ions, thereby facilitating more efficient degradation. On the other hand, at higher pH values, reduced degradation may be attributed to the formation of insoluble complexes, which decrease UV light penetration and, consequently, reduce hydroxyl radical generation potential. Additionally, Zeta potential measurements for  $\text{CuFe}_{12}\text{O}_{19}$  were performed at various pH values to support these observations. The Zeta potential values at pH 1, 3, 5, 7, and 11 were found to be +16.3, +7.4, -2.2, -6.8, and -19.6 mV, respectively. These values indicate the change in surface charge of the catalyst with pH, which is consistent with the proposed electrostatic repulsion mechanism between the catalyst and the antibiotic at higher pH values.

### 3.8.2. Effect of $\text{CuFe}_{12}\text{O}_{19}$ concentration

Another significant factor influencing pollutant degradation is the nanocatalyst concentration.  $\text{CuFe}_{12}\text{O}_{19}$  concentrations between 0.2 and 1.7 g/L were evaluated at the optimal pH of 5 for Penicillin G degradation, with the results presented in Fig. 9. The data indicate that degradation efficiency increases with catalyst concentration up to a certain level. Notably, increasing the concentration from 0.2 g/L to 0.8 g/L enhanced the degradation efficiency from 56.17% to 67.43%. However, at concentrations above 0.8 g/L, the efficiency declined, reaching 47.38% at 1.7 g/L. This trend can be related to two main factors. Initially, increasing the catalyst concentration enhances the availability of active sites and the generation of reactive oxygen species (ROS), leading to improved degradation. However, at higher concentrations, particle aggregation occurs due to the magnetic nature of  $\text{CuFe}_{12}\text{O}_{19}$ , reducing the active surface area [3]. Additionally, excessive catalyst loading can limit

light penetration, further decreasing degradation efficiency. Therefore, 0.8 g/L is considered the optimal concentration for Penicillin G degradation, balancing catalytic activity and minimizing unwanted side effects.

### 3.8.3. Effect of antibiotic concentration

After determining the optimal pH and nanocatalyst concentration in the previous steps, this stage focused on evaluating the effect of penicillin G concentration to establish the most favorable conditions. Penicillin G concentrations of 20, 40, 60, and 80 ppm were studied, with the results presented in [Figure 10](#). The findings illustrate that the degradation efficiency of Penicillin G decreased as the antibiotic concentration increased. The best degradation was observed at 20 ppm (73.27%), whereas the lowest efficiency (40.02%) was recorded at 80 ppm. This decline in degradation efficiency can be attributed to increased light absorption by the antibiotic molecules. As the antibiotic concentration rises, more light is absorbed by the antibiotic itself, reducing the amount of light reaching the nanocatalyst. Consequently, fewer photons interact with the catalyst surface, leading to a lower degradation rate.

### 3.8.4. Photocatalytic performance of $\text{CuFe}_{12}\text{O}_{19}@\text{ZnO}$ and $\text{CuFe}_{12}\text{O}_{19}@\text{ZnO}/\text{Au}$

In previous experiments, the optimal catalyst concentration, penicillin G concentration, and pH, using magnetic  $\text{CuFe}_{12}\text{O}_{19}$  nanocatalysts were determined. To further investigate the synergistic role of ZnO and Au NPs in enhancing photocatalytic efficiency, Penicillin G degradation was examined using  $\text{CuFe}_{12}\text{O}_{19}@\text{ZnO}$  and  $\text{CuFe}_{12}\text{O}_{19}@\text{ZnO}/\text{Au}$  under UV light under optimized conditions. The results, presented in [Figure 11](#), show an 83.56% degradation efficiency after 140 min when ZnO was deposited onto the  $\text{CuFe}_{12}\text{O}_{19}$  substrate. Incorporating Au nanoparticles into the  $\text{CuFe}_{12}\text{O}_{19}@\text{ZnO}$  structure further increased the degradation efficiency to 89.61%. This improvement can be attributed to several synergistic effects: (i) Enhanced charge separation: The presence of Au facilitates electron transfer from ZnO, reducing electron-hole recombination and increasing charge carrier lifespan. (ii)

Surface plasmon resonance effect of Au: This effect enables broader light absorption, enhancing photocatalytic performance. (iii) Reduced bandgap energy: The incorporation of Au lowers the bandgap of the nanocomposite, improving its efficiency under UV light. Additionally, ZnO provides active sites for the generation of hydroxyl ( $\text{OH}\cdot$ ) and superoxide ( $\text{O}_2^-$ ) radicals, which play a crucial role in Penicillin G degradation. These observations align with the measured reduction in bandgap energy, confirming the successful modification of the magnetic nanocatalyst. Overall, the synergistic effects of ZnO and Au significantly enhance the photocatalytic performance of the  $\text{CuFe}_{12}\text{O}_{19}$  NCs.

### 3.8.5. Photocatalytic mineralization

To evaluate the degree of mineralization during the photocatalytic degradation, both total chemical oxygen demand (COD) and organic carbon (TOC) were determined. The experiments were conducted under optimized conditions, which were previously determined, with a solution pH of 5, a catalyst dosage of 0.8 g/L, an initial antibiotic concentration of 20 ppm, and a reaction time of 140 min. TOC and COD are commonly used as key parameters to assess the mineralization of organic pollutants in advanced oxidation processes. The photocatalytic system achieved a TOC removal efficiency of 63.9%, while the COD removal was 76.3% (Fig. 12). The higher COD removal indicates that a significant portion of the organic contaminants was oxidized into simpler intermediates, which were ultimately mineralized into  $\text{CO}_2$  and  $\text{H}_2\text{O}$ . The remaining TOC suggests that some carbon-based intermediates were still present in the solution. The results also show that most of the reduction in both TOC and COD occurred within the first 80 min of the reaction, likely due to the rapid degradation of aromatic rings by reactive oxygen species [34]. Extending the reaction time may further enhance COD removal and improve the overall mineralization efficiency of the photocatalytic process.

### 3.8.6. Mechanism of antibiotic degradation

The proposed degradation mechanism in the  $\text{CuFe}_{12}\text{O}_{19}@Z\text{nO}/\text{Au}$  nanocomposite system is based on general principles observed in similar metal-semiconductor photocatalytic systems, such as those

reported in the literature for  $\text{Fe}_3\text{O}_4@\text{TiO}_2\text{-Au}$  composites [35]. Although the components of these systems differ, particularly in the use of  $\text{TiO}_2$  instead of  $\text{ZnO}$ , the underlying photocatalytic mechanism, where electron transfer occurs from the semiconductor to metal nanoparticles ( $\text{Au}$ ), could be similar. In this study, we hypothesize that a comparable mechanism may be occurring in the  $\text{CuFe}_{12}\text{O}_{19}@\text{ZnO}/\text{Au}$  system (Fig. 13). Upon UV light exposure, photoexcited electrons from  $\text{ZnO}$  conduction band migrate to the gold nanoparticles, causing a shift in the composite overall Fermi level ( $E_f$ ) to a more negative potential ( $E_f^*$ ). The electron transfer is enhanced by the formation of a Schottky junction at the metal-semiconductor interface. Gold nanoparticles act as electron acceptors, enhancing charge separation and prolonging the lifetime of the electron-hole pairs, which in turn promotes photocatalytic activity. These transferred electrons are captured by adsorbed oxygen ( $\text{O}_2$ ), leading to the generation of reactive oxygen species such as superoxide anion radicals ( $\text{O}_2^-$ ) and hydroxyl radicals ( $\text{OH}^\cdot$ ), which are highly effective in degrading Penicillin G. The magnetic properties of  $\text{CuFe}_{12}\text{O}_{19}$  can facilitate the separation and retention of the catalyst after the reaction, which can be advantageous for catalyst recycling and stability. Furthermore, the magnetic nature of  $\text{CuFe}_{12}\text{O}_{19}$  helps to enhance the overall photocatalytic performance of the  $\text{CuFe}_{12}\text{O}_{19}@\text{ZnO}/\text{Au}$  nanocomposite by improving the charge carrier separation, which leads to increased degradation efficiency.

### 3.9. Recyclability and photocatalytic stability of $\text{CuFe}_{12}\text{O}_{19}@\text{ZnO}/\text{Au}$ NCs

The recyclability and photocatalytic stability of the  $\text{CuFe}_{12}\text{O}_{19}@\text{ZnO}/\text{Au}$  NCs were investigated by evaluating its performance in degrading the penicillin G over five consecutive cycles. The results, shown in Fig. 14, demonstrate that the photocatalyst retained a substantial portion of its activity. Specifically, 89.61% of the antibiotic was degraded after the first cycle, with only a slight decrease to 79.42% degradation observed after five cycles. This minimal reduction in photocatalytic efficiency indicates the robustness and stability of the  $\text{CuFe}_{12}\text{O}_{19}@\text{ZnO}/\text{Au}$  NCs under repeated use. Such recyclability highlights its potential for practical applications in wastewater treatment, where durability and efficiency over multiple cycles are critical requirements. The ability to maintain high

degradation rates even after successive cycles underscores the nanocomposite's suitability as a sustainable photocatalyst for environmental remediation.

#### **4. Conclusion**

In this research,  $\text{CuFe}_{12}\text{O}_{19}@\text{ZnO}/\text{Au}$  NCs were synthesized, exhibiting a high photocatalytic degradation efficiency of 89.61% for Penicillin G under optimized conditions (pH 5, 0.8 g/L catalyst concentration, and 20 ppm antibiotic). This performance outperformed that of the individual components,  $\text{CuFe}_{12}\text{O}_{19}$  and  $\text{CuFe}_{12}\text{O}_{19}@\text{ZnO}$ . The enhanced degradation efficiency was related to the synergistic effects of ZnO and Au, which facilitated improved electron transfer, reduced recombination of electron-hole pairs, and enhanced UV light absorption. Furthermore, antibacterial tests demonstrated that the  $\text{CuFe}_{12}\text{O}_{19}@\text{ZnO}/\text{Au}$  nanocomposite showed superior activity against Gram-negative bacteria, due to the enhanced interaction between the nanocomposite and the thinner peptidoglycan layer of Gram-negative bacteria.

## References

- [1] N. Zulfiqar, R. Nadeem, O.A.I. Musaimi, Photocatalytic Degradation of Antibiotics via Exploitation of a Magnetic Nanocomposite: A Green Nanotechnology Approach toward Drug-Contaminated Wastewater Reclamation, *ACS Omega*, 9 (2024) 7986-8004.
- [2] E. Baladi, F. Davar, A. Hojjati-Najafabadi, Synthesis and characterization of g-C<sub>3</sub>N<sub>4</sub>-CoFe<sub>2</sub>O<sub>4</sub>-ZnO magnetic nanocomposites for enhancing photocatalytic activity with visible light for degradation of penicillin G antibiotic, *Environmental Research*, 215 (2022) 114270.
- [3] M. Kamranifar, A. Allahresani, A. Naghizadeh, Synthesis and characterizations of a novel CoFe<sub>2</sub>O<sub>4</sub>@CuS magnetic nanocomposite and investigation of its efficiency for photocatalytic degradation of penicillin G antibiotic in simulated wastewater, *Journal of Hazardous Materials*, 366 (2019) 545-555.
- [4] M. Berkani, A. Smaali, Y. Kadmi, F. Almomani, Y. Vasseghian, N. Lakhdari, M. Alyane, Photocatalytic degradation of Penicillin G in aqueous solutions: Kinetic, degradation pathway, and microbioassays assessment, *Journal of Hazardous Materials*, 421 (2022) 126719.
- [5] A.I. Merchant, A.H. Vakili, A. Kocaman, S.S. Abu Amr, New advancement of advanced oxidation processes for the treatment of Petroleum wastewater, *Desalination and Water Treatment*, 319 (2024) 100565.
- [6] H. Salari, Efficient photocatalytic degradation of environmental pollutant with enhanced photocarrier separation in novel Z-scheme  $\alpha$ -MnO<sub>2</sub> nanorod/ $\alpha$ -MoO<sub>3</sub> nanocomposites, *Journal of Photochemistry and Photobiology A: Chemistry*, 401 (2020) 112787.
- [7] A. Soukeur, M.M. Kaci, S. Omeiri, B. Bellal, M. Amara, M. Trari, Photocatalytic degradation of bromothymol blue over MgFe<sub>2</sub>O<sub>4</sub> under sunlight exposure, *Optical Materials*, 142 (2023) 114108.
- [8] M.M. Kaci, N. Nasrallah, F. Atmani, M. Kebir, R. Guernanou, A. Soukeur, M. Trari, Enhanced photocatalytic performance of CuAl<sub>2</sub>O<sub>4</sub> nanoparticles spinel for dye degradation under visible light, *Research on Chemical Intermediates*, 47 (2021) 3785-3806.

- [9] K. Derkaoui, I. Bencherifa, T. Hadjersi, I. Belkhettab, K. Boukhoudem, S. Bouanik, A. Brik, M. Kechouane, M.M. Kaci, MnO<sub>2</sub> decorated silicon nanowires: A novel photocatalyst for improved Rhodamine B removal under visible light exposure, *Surfaces and Interfaces*, 53 (2024) 105086.
- [10] F. Ansari, A. Sobhani, M. Salavati-Niasari, Facile synthesis, characterization and magnetic property of CuFe<sub>2</sub>O<sub>4</sub> nanostructures via a sol–gel auto-combustion process, *Journal of Magnetism and Magnetic Materials*, 401 (2016) 362-369.
- [11] M. Mahdiani, F. Soofivand, F. Ansari, M. Salavati-Niasari, Grafting of CuFe<sub>2</sub>O<sub>4</sub> nanoparticles on CNT and graphene: Eco-friendly synthesis, characterization and photocatalytic activity, *Journal of Cleaner Production*, 176 (2018) 1185-1197.
- [12] M. Mahdiani, A. Sobhani, M. Salavati-Niasari, Enhancement of magnetic, electrochemical and photocatalytic properties of lead hexaferrites with coating graphene and CNT: Sol-gel auto-combustion synthesis by valine, *Separation and Purification Technology*, 185 (2017) 140-148.
- [13] T.M.H. Dang, V.D. Trinh, D.H. Bui, M.H. Phan, D.C. Huynh, Sol–gel hydrothermal synthesis of strontium hexaferrite nanoparticles and the relation between their crystal structure and high coercivity properties, *Advances in Natural Sciences: Nanoscience and Nanotechnology*, 3 (2012) 025015.
- [14] X. Tang, R.Y. Hong, W.G. Feng, D. Badami, Ethylene glycol assisted hydrothermal synthesis of strontium hexaferrite nanoparticles as precursor of magnetic fluid, *Journal of Alloys and Compounds*, 562 (2013) 211-218.
- [15] J. Liu, H. Wang, H. Wu, Y. Yang, C. Wang, Q. Wang, B. Jia, J. Zheng, Research progress on zinc oxide-based heterojunction photocatalysts, *Journal of Materials Chemistry A*, 12 (2024) 20838-20867.
- [16] A. Baig, M. Siddique, S. Panchal, A Review of Visible-Light-Active Zinc Oxide Photocatalysts for Environmental Application, *Catalysts*, 15 (2025) 100.

- [17] J.M. Wessels, H.-G. Nothofer, W.E. Ford, F. von Wrochem, F. Scholz, T. Vossmeier, A. Schroedter, H. Weller, A. Yasuda, Optical and Electrical Properties of Three-Dimensional Interlinked Gold Nanoparticle Assemblies, *Journal of the American Chemical Society*, 126 (2004) 3349-3356.
- [18] H. Pujiarti, R. Hidayat, P. Wulandari, Enhanced efficiency in dye-sensitized solar cell by localized surface plasmon resonance effect of gold nanoparticles, *Journal of Nonlinear Optical Physics & Materials*, 28 (2019) 1950040.
- [19] M. Ahlawat, D. Mittal, V. Govind Rao, Plasmon-induced hot-hole generation and extraction at nano-heterointerfaces for photocatalysis, *Communications Materials*, 2 (2021) 114.
- [20] L. Chen, L. Tian, X. Zhao, Z. Hu, J. Fan, K. Lv, SPR effect of Au nanoparticles on the visible photocatalytic RhB degradation and NO oxidation over TiO<sub>2</sub> hollow nanoboxes, *Arabian Journal of Chemistry*, 13 (2020) 4404-4416.
- [21] S. Mohammadi-Aghdam, F. Bahraini, S.M. Ghoreishi, In-vitro anticancer on acute lymphoblastic leukemia NALM-6 cell line, antibacterial and catalytic performance of eco-friendly synthesized ZnO and Ag-doped ZnO nanoparticles using *Hedera colchica* extract, *Biomass Conversion and Biorefinery*, 14 (2024) 20037-20052.
- [22] Z. Kiani, S. Mirjalili, K. Heydaryan, P. Mohammadparast, H. Aramjoo, F. Bahraini, A. Yousefinia, M. Torabi, S.M. Ghoreishi, M. Fattahi, S. Mortazavi-Derazkola, Harmonizing nature and nanotechnology: Phytoextract-mediated synthesis of Ag-doped ZnO nanoparticles using *Lavandula stoechas* extract for environmental and biomedical applications, *Journal of Drug Delivery Science and Technology*, 96 (2024) 105708.
- [23] C. Marcucci, J.M.A. Relats, H.G. Bach, F. Kamecki, B.G. Varela, M.L. Wagner, V. Pastore, N. Colettis, R.A. Ricco, M. Marder, Neurobehavioral evaluation and phytochemical characterization of a series of argentine valerian species, *Heliyon*, 6 (2020) e05691.

- [24] B. Sundararajan, B.D. Ranjitha Kumari, Novel synthesis of gold nanoparticles using *Artemisia vulgaris* L. leaf extract and their efficacy of larvicidal activity against dengue fever vector *Aedes aegypti* L, *Journal of Trace Elements in Medicine and Biology*, 43 (2017) 187-196.
- [25] D.E. Mazouzi, F. Djani, A. Soukeur, W. Bouchal, A. Manseri, K. Derkaoui, A. Martínez-Arias, A. Ksouri, F. Şen, M.M. Kaci, Auto-combustion designed BiFeO<sub>3</sub>/Bi<sub>2</sub>O<sub>3</sub> photocatalyst for improved photodegradation of nitrobenzene under visible light and sunlight irradiation, *Surfaces and Interfaces*, 44 (2024) 103581.
- [26] I. Akkari, Z. Graba, M. Pazos, N. Bezzi, A. Manseri, K. Derkaoui, M.M. Kaci, NaOH-activated Pomegranate Peel Hydrochar: Preparation, Characterization and Improved Acebutolol Adsorption, *Water, Air, & Soil Pollution*, 234 (2023) 705.
- [27] A.F. Jaramillo, R. Baez-Cruz, L.F. Montoya, C. Medinam, E. Pérez-Tijerina, F. Salazar, D. Rojas, M.F. Melendrez, Estimation of the surface interaction mechanism of ZnO nanoparticles modified with organosilane groups by Raman Spectroscopy, *Ceramics International*, 43 (2017) 11838-11847.
- [28] A.K. Alzubaidi, W.J. Al-Kaabi, A.A. Ali, S. Albukhaty, H. Al-Karagoly, G.M. Sulaiman, M. Asiri, Y. Khane, Green Synthesis and Characterization of Silver Nanoparticles Using Flaxseed Extract and Evaluation of Their Antibacterial and Antioxidant Activities, *Applied Sciences*, 13 (2023) 2182.
- [29] B. Javidan, P. Gharbani, Synthesis of copper hexaferrite magnetic nanoparticles based on carboxymethyl cellulose modified with polyacrylic acid (CMC/PAA/CuFe<sub>12</sub>O<sub>19</sub>) for loading and release of Levothyroxine, *International Journal of Biological Macromolecules*, 282 (2024) 137040.
- [30] M. Asri, A. Naghizadeh, A. Hasani, S. Mortazavi-Derazkola, A. Javid, F. Masoudi, Sustainable green synthesis of ZnFe<sub>2</sub>O<sub>4</sub>@ZnO nanocomposite using Oleaster tree bark methanolic extract for photocatalytic degradation of aqueous humic acid in the presence of UVc irradiation, *AQUA - Water Infrastructure, Ecosystems and Society*, 72 (2023) 1800-1814.
- [31] M. Luna, M. Barawi, S. Gómez-Moñivas, J. Colchero, M. Rodríguez-Peña, S. Yang, X. Zhao, Y.-H. Lu, R. Chintala, P. Reñones, V. Altoe, L. Martínez, Y. Huttel, S. Kawasaki, A. Weber-Bargioni,

V.A. de la Peña ÓShea, P. Yang, P.D. Ashby, M. Salmeron, Photoinduced Charge Transfer and Trapping on Single Gold Metal Nanoparticles on TiO<sub>2</sub>, ACS Applied Materials & Interfaces, 13 (2021) 50531-50538.

[32] M. Zare-Bidaki, P. Mohammadparast-Tabas, M. Khorashadizade, P. Mohammadparast-Tabas, E. Alemzadeh, A. Saberi, H. Kabiri-Rad, S. Eghbali, Bio-synthesized AGS@AgNPs for wound healing, antioxidant support, antibacterial defense, and anticancer intervention, Biocatalysis and Agricultural Biotechnology, 61 (2024) 103402.

[33] N.M. Hussein, S. Mortazavi-Drazkola, Tunable hierarchical novel ZnFe<sub>2</sub>O<sub>4</sub>-based magnetic nanocomposites: Synergistic TiO<sub>2</sub> integration and Au enhancement for efficient antibiotic degradation and antibacterial applications, Colloids and Surfaces A: Physicochemical and Engineering Aspects, 714 (2025) 136585.

[34] T.J. Al-Musawi, P. Rajiv, N. Mengelizadeh, F. Sadat Arghavan, D. Balarak, Photocatalytic efficiency of CuNiFe<sub>2</sub>O<sub>4</sub> nanoparticles loaded on multi-walled carbon nanotubes as a novel photocatalyst for ampicillin degradation, Journal of Molecular Liquids, 337 (2021) 116470.

[35] J. Ma, S. Guo, X. Guo, H. Ge, A mild synthetic route to Fe<sub>3</sub>O<sub>4</sub>@TiO<sub>2</sub>-Au composites: preparation, characterization and photocatalytic activity, Applied Surface Science, 353 (2015) 1117-1125.

## Figure captions

**Table.1.** Various conditions for photocatalytic reactions under different parameters.

**Table.2.** Antibacterial activity results of  $\text{CuFe}_{12}\text{O}_{19}$ ,  $\text{CuFe}_{12}\text{O}_{19}@ZnO$ , and  $\text{CuFe}_{12}\text{O}_{19}@ZnO/Au$  nanocomposites against various strains.

**Fig.1.** Proposed mechanism for the formation of  $\text{CuFe}_{12}\text{O}_{19}@ZnO/Au$  nanocomposites in the presence of plant extract.

**Fig.2.** XRD patterns of synthesized nanomaterials: (a)  $\text{CuFe}_{12}\text{O}_{19}$ , (b)  $\text{CuFe}_{12}\text{O}_{19}@ZnO$ , and (c)  $\text{CuFe}_{12}\text{O}_{19}@ZnO/Au$  nanocomposites.

**Fig.3.** FTIR spectra of (a)  $\text{CuFe}_{12}\text{O}_{19}$ , (b)  $\text{CuFe}_{12}\text{O}_{19}@ZnO$ , and (c)  $\text{CuFe}_{12}\text{O}_{19}@ZnO/Au$  nanocomposites.

**Fig.4.** TEM images and corresponding histogram plots of (a)  $\text{CuFe}_{12}\text{O}_{19}$ , (b)  $\text{CuFe}_{12}\text{O}_{19}@ZnO$ , and (c)  $\text{CuFe}_{12}\text{O}_{19}@ZnO/Au$  nanocomposites.

**Fig.5.** VSM analysis for investigating magnetic properties of ((a)  $\text{CuFe}_{12}\text{O}_{19}$ , (b)  $\text{CuFe}_{12}\text{O}_{19}@ZnO$ , and (c)  $\text{CuFe}_{12}\text{O}_{19}@ZnO/Au$  nanocomposites.

**Fig.6.** Diffuse reflectance spectroscopy of (a)  $\text{CuFe}_{12}\text{O}_{19}$ , (b)  $\text{CuFe}_{12}\text{O}_{19}@ZnO$ , and (c)  $\text{CuFe}_{12}\text{O}_{19}@ZnO/Au$  nanocomposites.

**Fig.7.** Proposed mechanism for the antibacterial activity of  $\text{CuFe}_{12}\text{O}_{19}@ZnO/Au$  nanocomposite against bacteria

**Fig.8.** Degradation of penicillin G at different pH values using  $\text{CuFe}_{12}\text{O}_{19}$ .

**Fig.9.** Degradation of penicillin G at different nanocatalyst dosage values using  $\text{CuFe}_{12}\text{O}_{19}$ .

**Fig.10.** Degradation of penicillin G at various antibiotic concentration using  $\text{CuFe}_{12}\text{O}_{19}$ .

**Fig.11** Photocatalytic activity of  $\text{CuFe}_{12}\text{O}_{19}@ZnO$  and  $\text{CuFe}_{12}\text{O}_{19}@ZnO/Au$  nanocomposites under optimal conditions.

**Fig.12.** COD and TOC removal of penicillin G under optimized circumstances.

**Fig.13.** Possible mechanism for antibiotic degradation using  $\text{CuFe}_{12}\text{O}_{19}@ZnO/Au$  nanocomposites.

**Fig.14.** Reusability of the  $\text{CuFe}_{12}\text{O}_{19}@ZnO/Au$  nanocomposites.

**Table.1.**

<b>Sample no.</b>	<b>pH</b>	<b>Catalyst concentration (g/l)</b>	<b>Antibiotic concentration (ppm)</b>	<b>Figure</b>
1	1	0.5	40	Fig.8
2	3	0.5	40	Fig.8
3	5	0.5	40	Fig.8
4	7	0.5	40	Fig.8
5	11	0.5	40	Fig.8
6	5	0.2	40	Fig.9
7	5	0.8	40	Fig.9
8	5	1.1	40	Fig.9
9	5	1.4	40	Fig.9
10	5	1.7	40	Fig.9
11	5	0.8	20	Fig.10
12	5	0.8	60	Fig.10
13	5	0.8	80	Fig.10

**Table.2.**

<b>Strain</b>	<b>Extract</b>	<b>CuFe<sub>12</sub>O<sub>19</sub></b>	<b>CuFe<sub>12</sub>O<sub>19</sub>@ZnO</b>		<b>CuFe<sub>12</sub>O<sub>19</sub>@ZnO/Au</b>	
	<b>MIC</b>	<b>MIC</b>	<b>MIC</b>	<b>MBC</b>	<b>MIC</b>	<b>MBC</b>
	<b>(µg/ml)</b>	<b>(µg/ml)</b>	<b>(µg/ml)</b>	<b>(µg/ml)</b>	<b>(µg/ml)</b>	<b>(µg/ml)</b>
<i>S. aureus</i>	>8000	>4000	2000	4000	1000	2000
<i>E. faecalis</i>	>8000	>4000	2000	4000	1000	4000
<i>E. coli</i>	>8000	>4000	1000	2000	500	1000
<i>K. pneumoniae</i>	>8000	>4000	2000	4000	500	2000

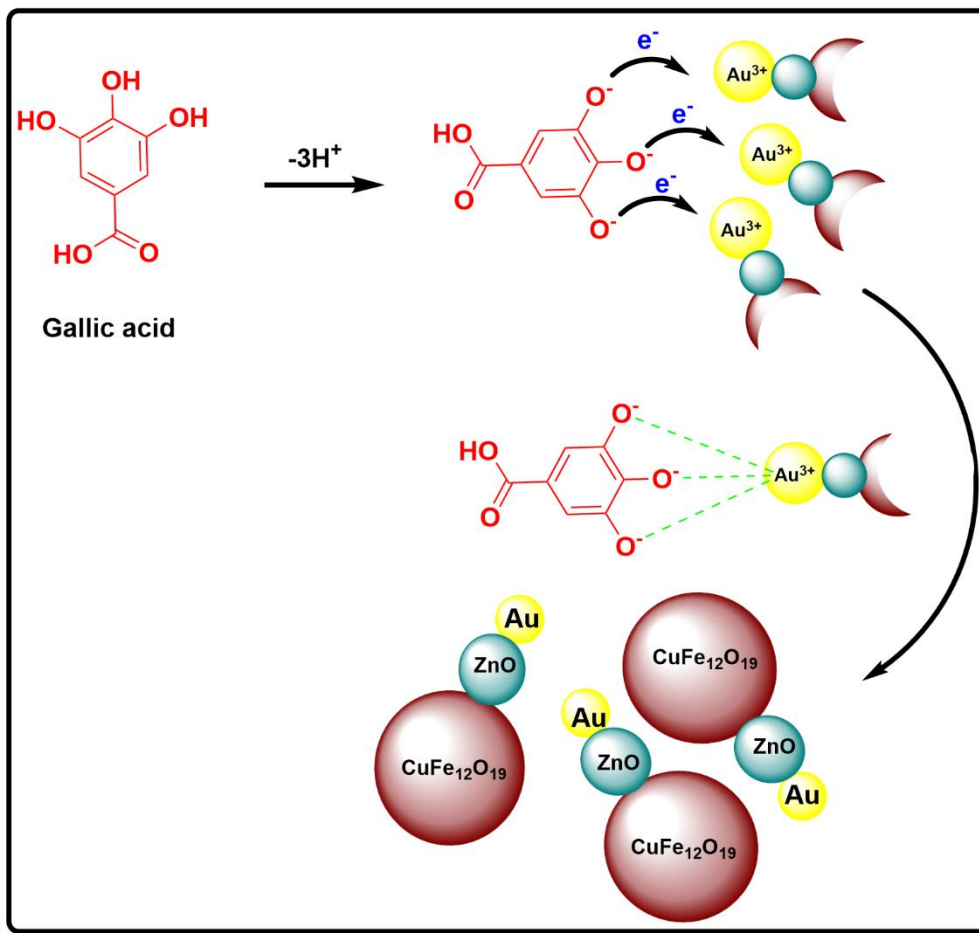


Fig.1.

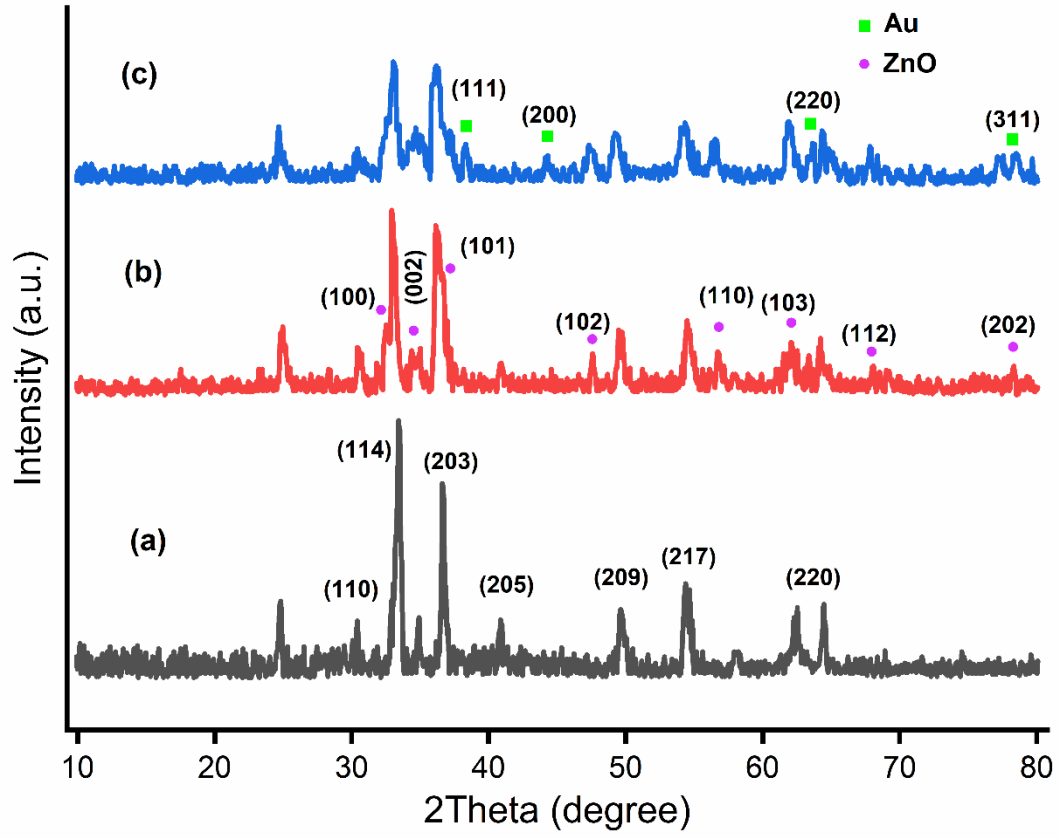


Fig.2.

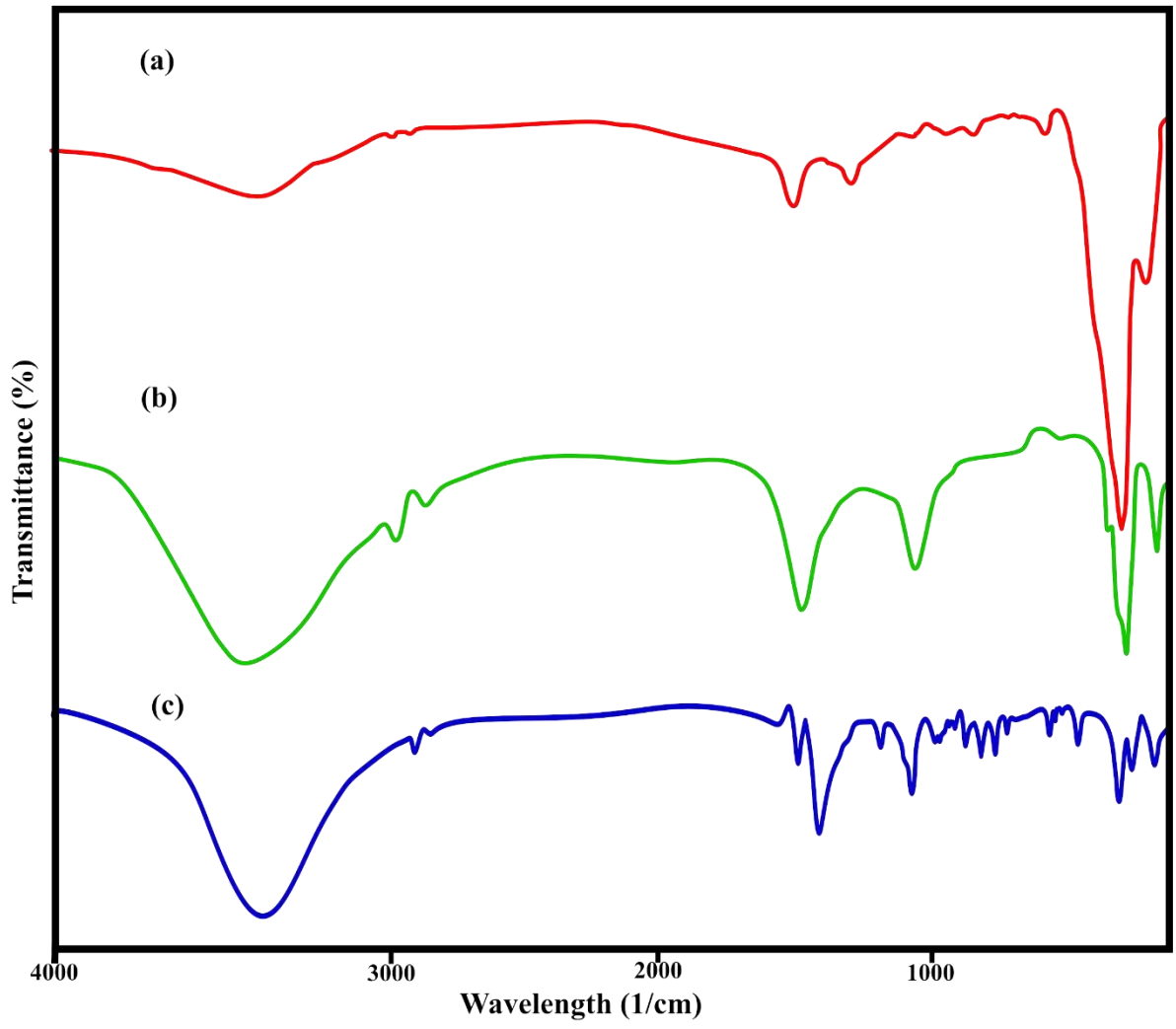


Fig.3.

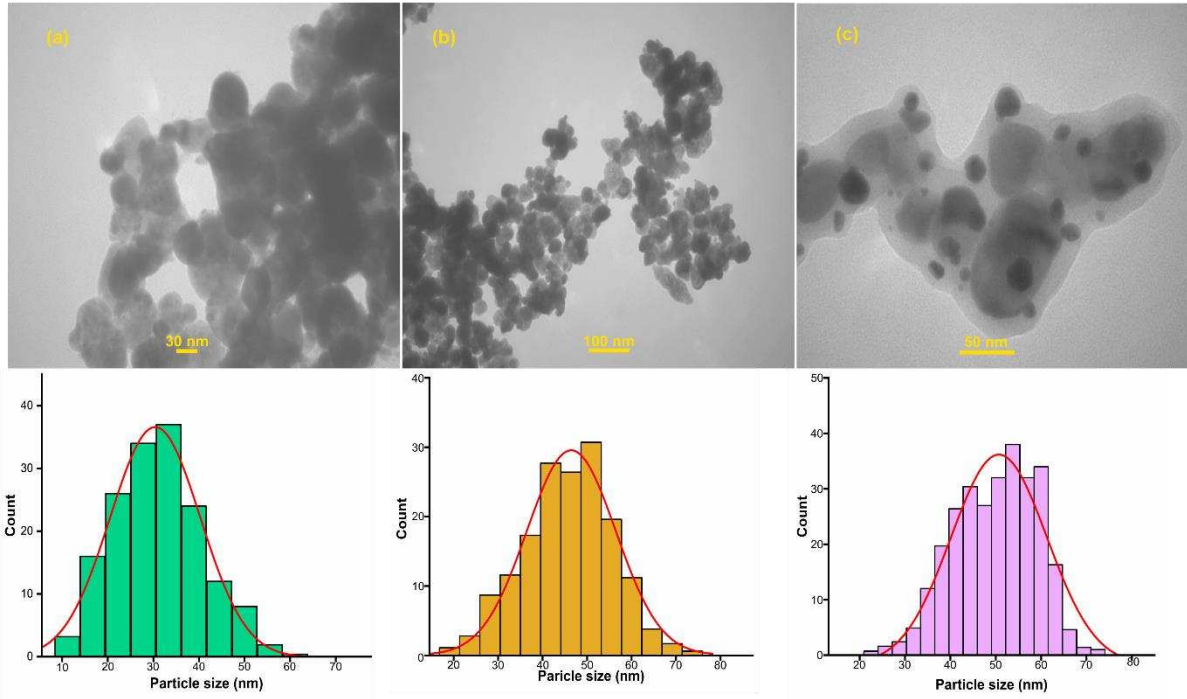


Fig.4.

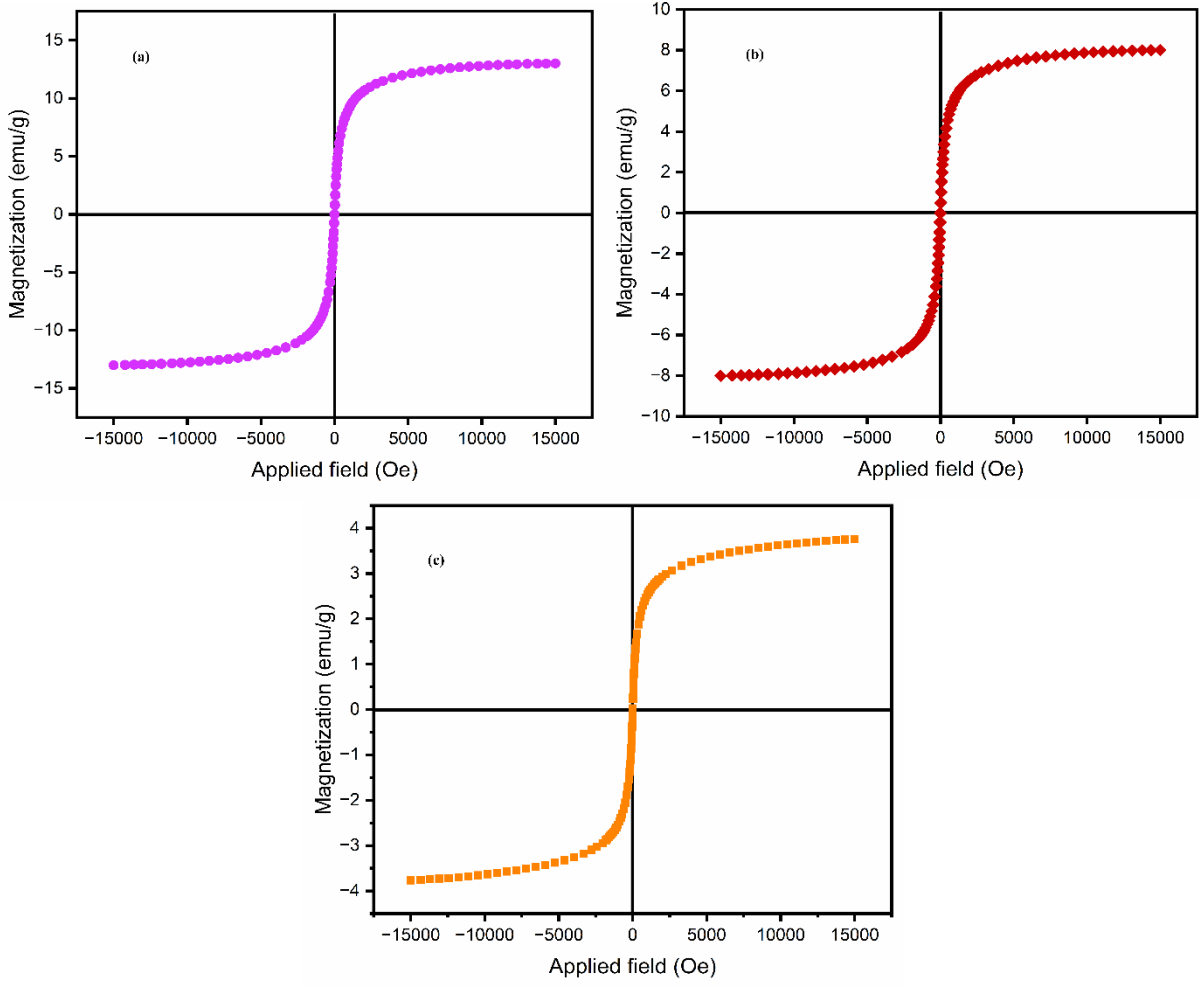


Fig.5.

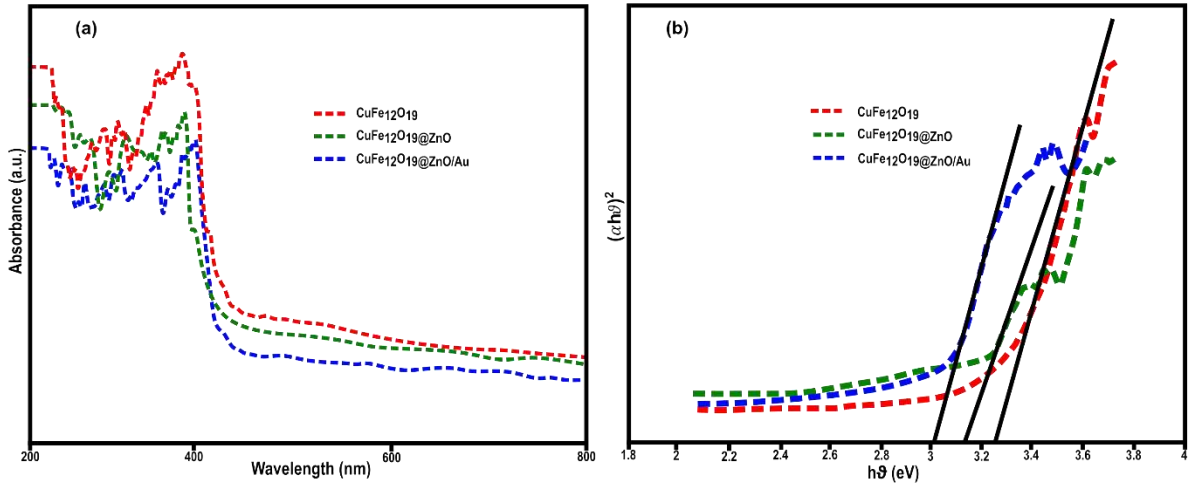


Fig.6.

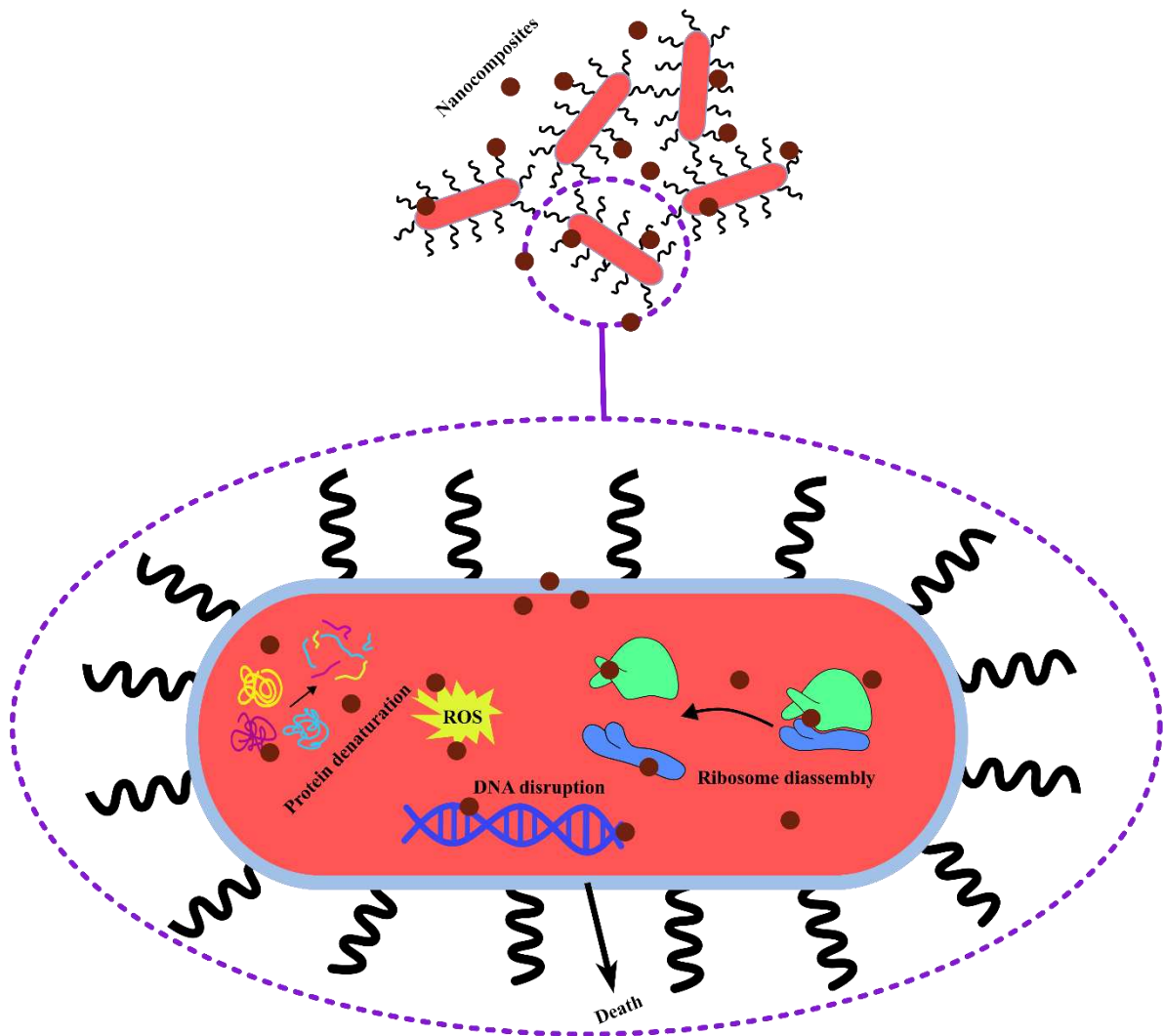


Fig.7.

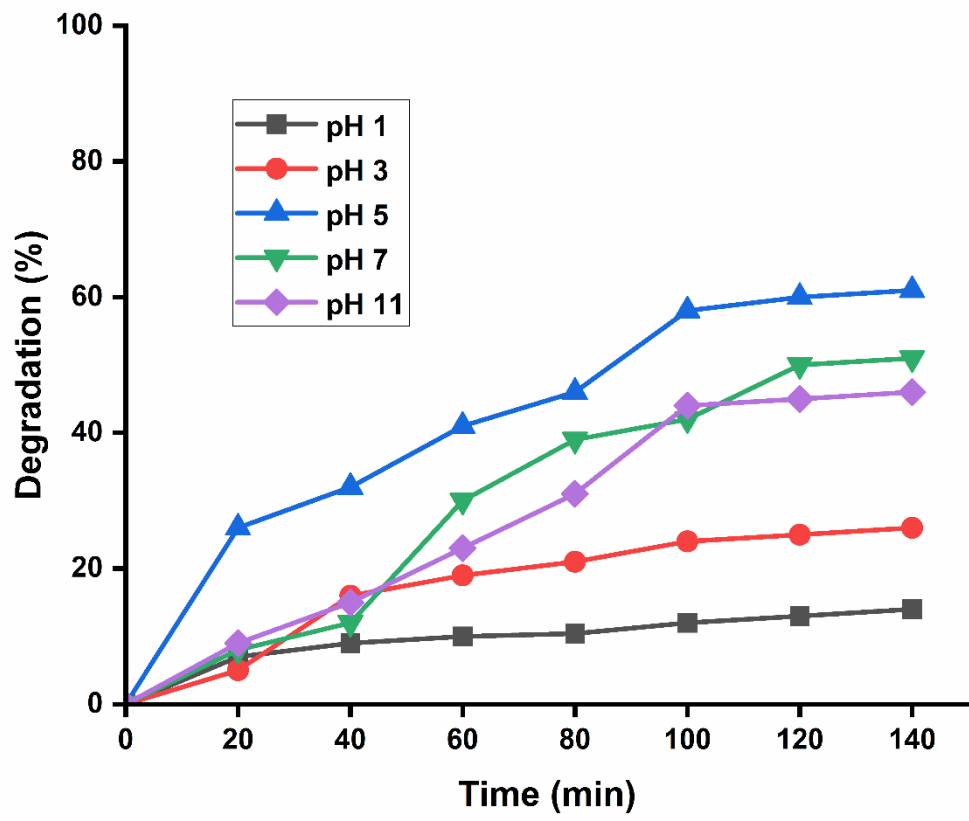


Fig.8.

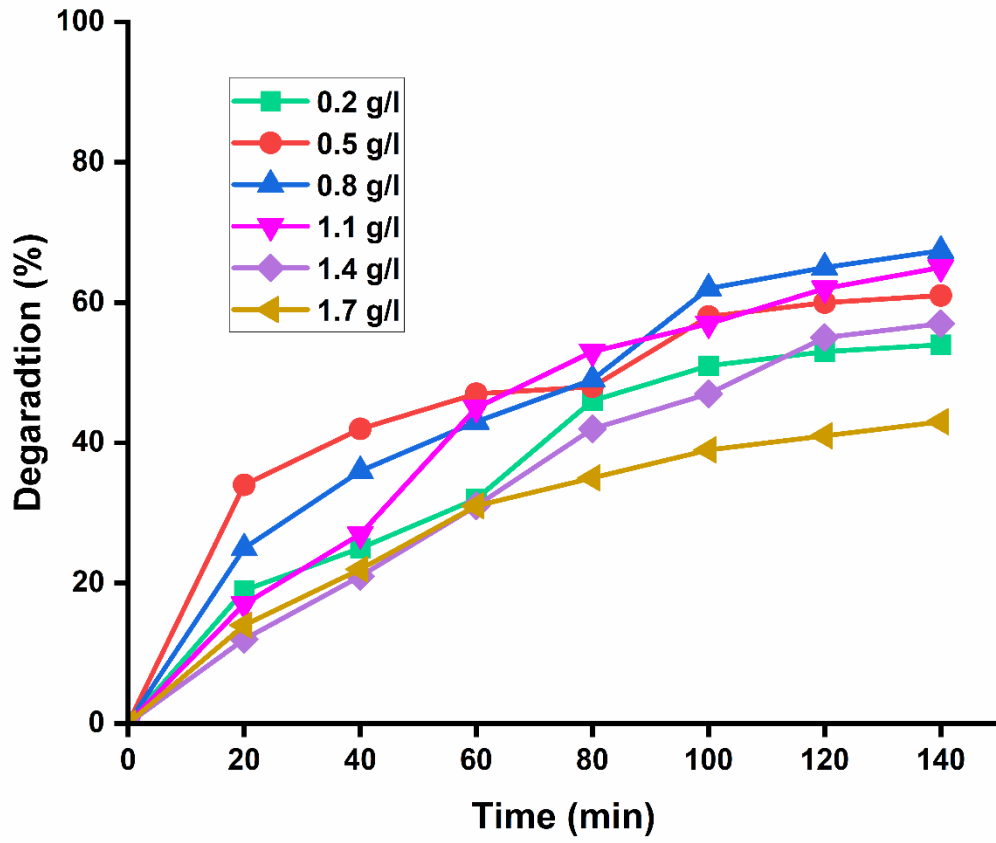


Fig.9.

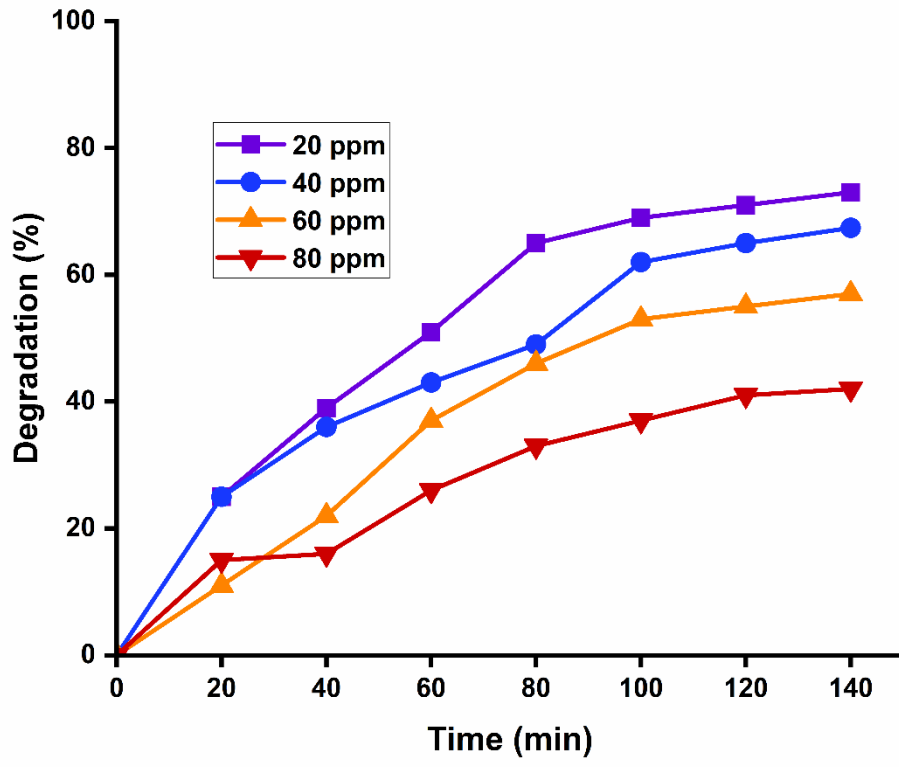


Fig.10.

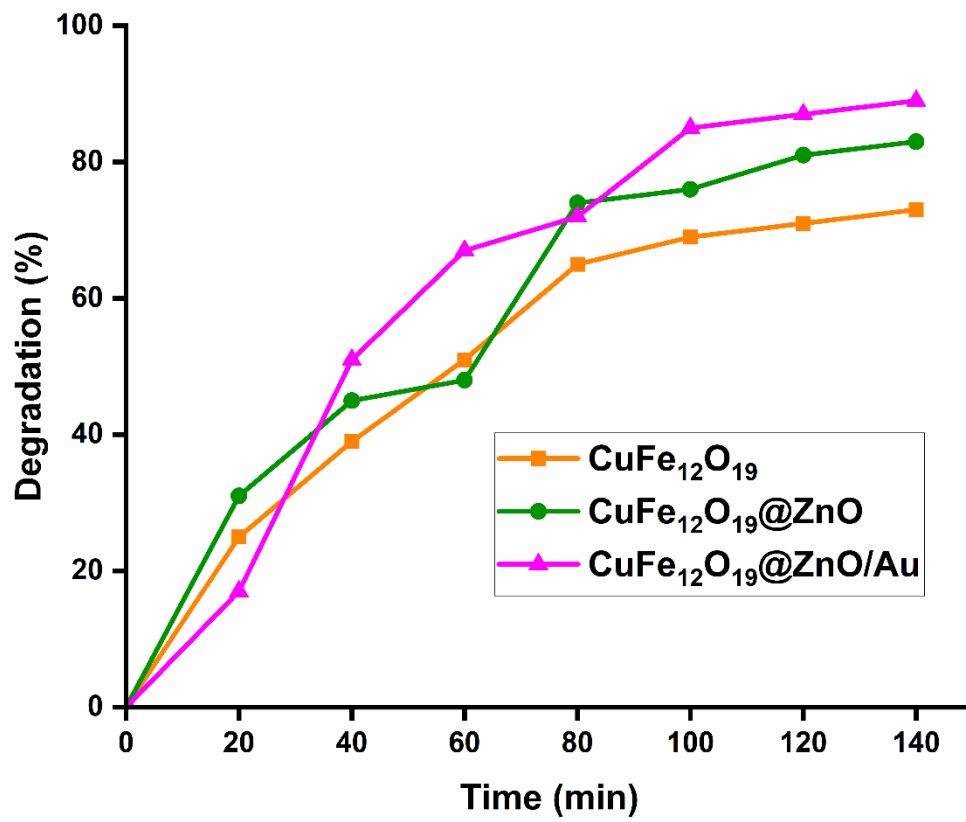


Fig.11.

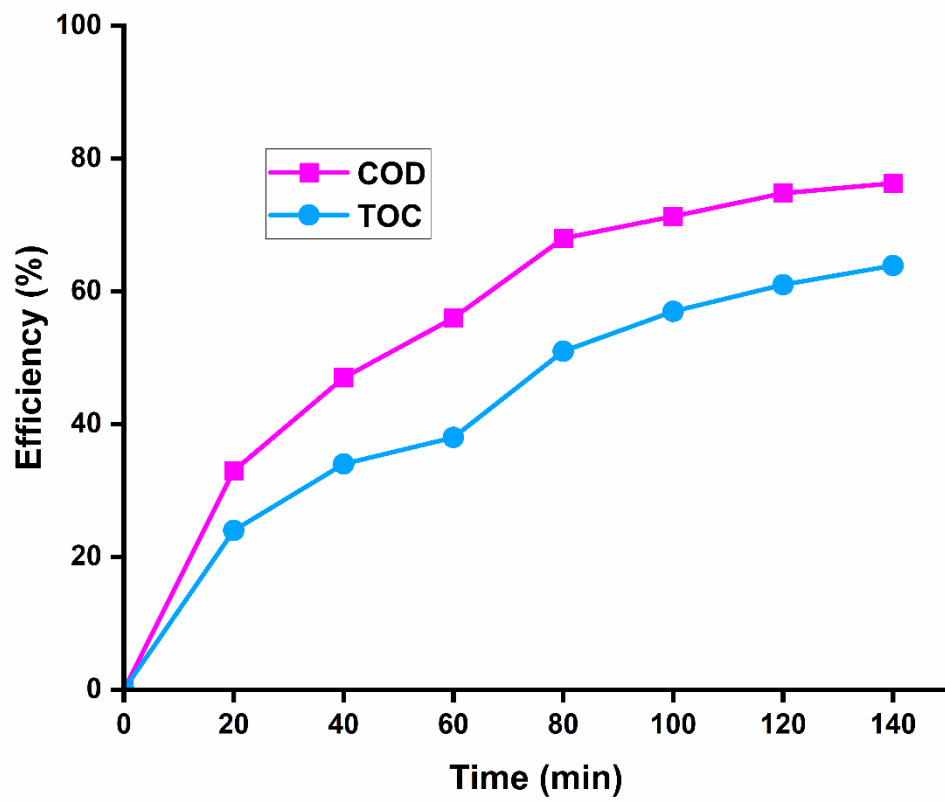


Fig.12.

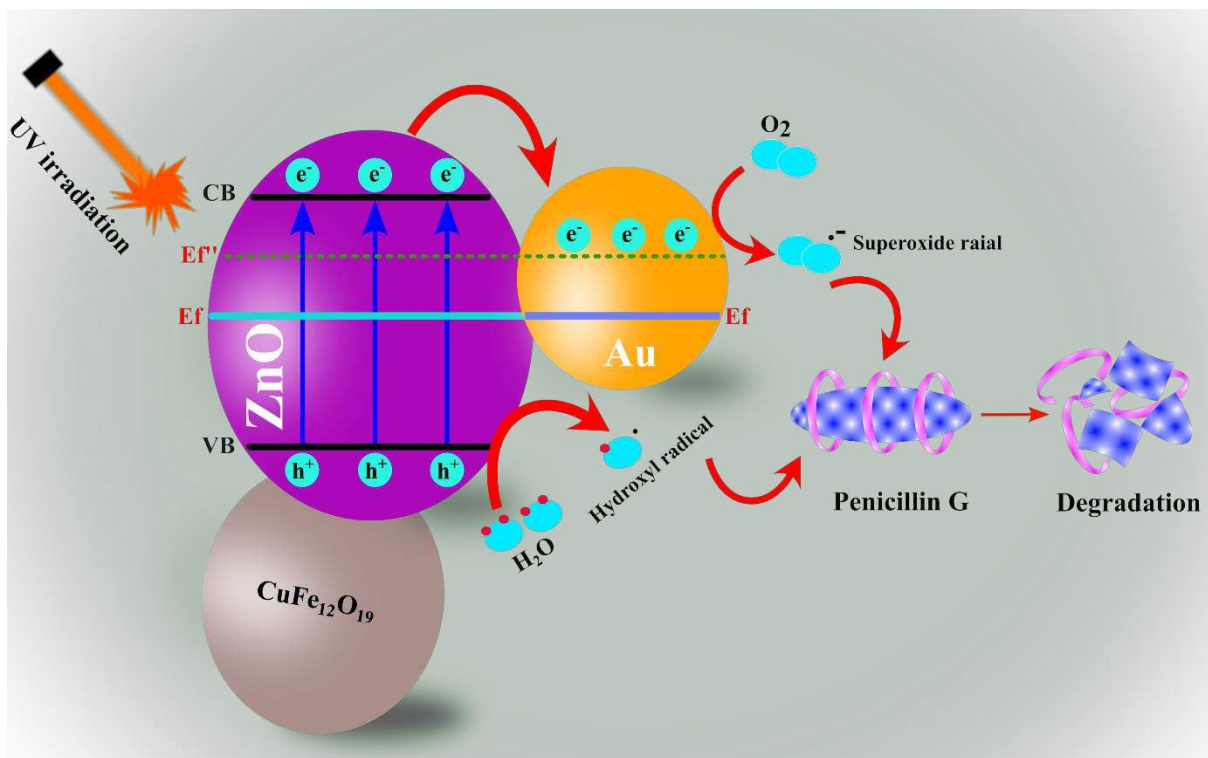


Fig.13.

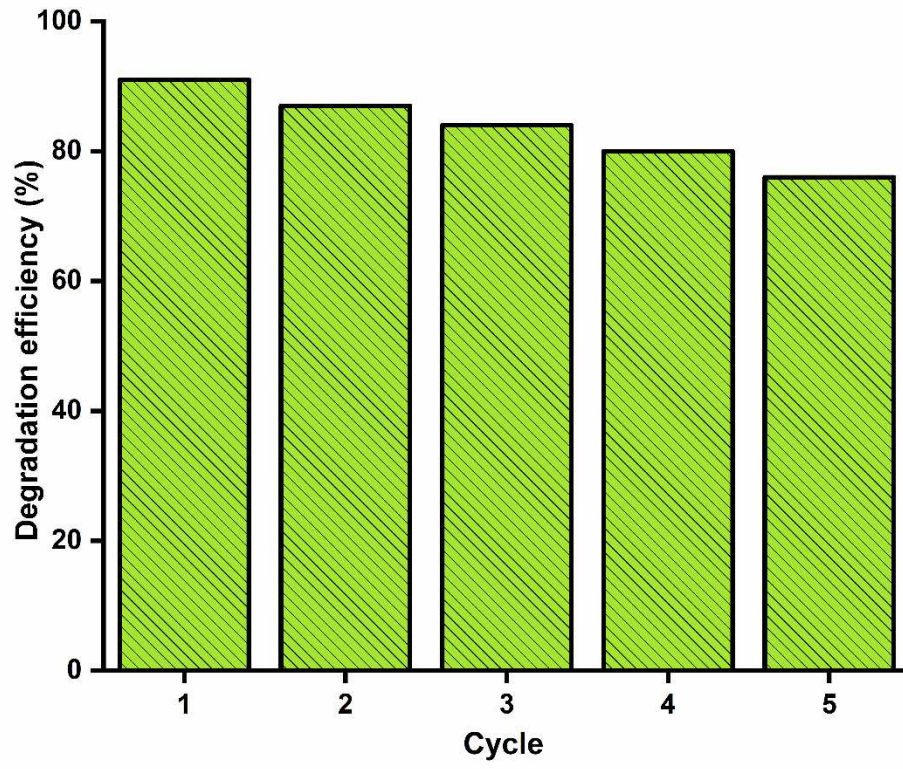


Fig.13.